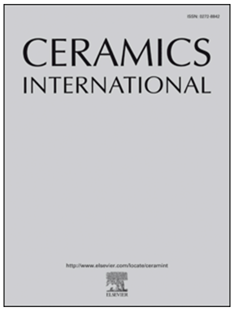

Structure and mechanical properties of nanofibrous ZrO_2 derived from alternating field electrospun precursors

Andrei Stanishevsky, Riley Yager, Jolanta Tomaszewska, Michał Binczarski, Waldemar Maniukiewicz, Izabela Witońska, David Lukas

PII: S0272-8842(19)31588-3
DOI: https://doi.org/10.1016/j.ceramint.2019.06.092
Reference: CERI 21901

To appear in: *Ceramics International*

Received Date: 30 December 2018
Revised Date: 17 May 2019
Accepted Date: 11 June 2019

Please cite this article as: A. Stanishevsky, R. Yager, J. Tomaszewska, Michał. Binczarski, W. Maniukiewicz, I. Witońska, D. Lukas, Structure and mechanical properties of nanofibrous ZrO_2 derived from alternating field electrospun precursors, *Ceramics International* (2019), doi: https://doi.org/10.1016/j.ceramint.2019.06.092.

CERI-D-18-12429 Revised R2

Structure and mechanical properties of nanofibrous ZrO_2 derived from alternating field electrospun precursors

Andrei Stanishevsky[1*], Riley Yager[1], Jolanta Tomaszewska[2], Michał Binczarski[2], Waldemar Maniukiewicz[3], Izabela Witońska[2], David Lukas[4]

[1] *Department of Physics, University of Alabama at Birmingham, 1300 University Boulevard, Birmingham, AL 35294-1170, USA*

[2] *Institute of General and Ecological Chemistry, Faculty of Chemistry, Lodz University of Technology, Zeromskiego 116, 90-924 Lodz, Poland*

[3] *Department of Semiconductor and Optoelectronics Devices, Lodz University of Technology, Wolczanska 211/215, 90-924 Lodz, Poland*

[4] *Faculty of Textile Engineering, Technical University of Liberec, Studentska 2, Liberec 1, 461 17, Czech Republic*

**Corresponding author:*

Andrei Stanishevsky

Email: astan@uab.edu

Tel: +205-934-8030

Department of Physics,

University of Alabama at Birmingham,

1300 University Boulevard, CH 342,

Birmingham, AL 35294-1170, USA

ABSTRACT

Nanofibrous zirconia (ZrO_2) meshes were prepared from precursor fibers which were synthesized using the method of free-surface, high-yield alternating field electrospinning (AFES). The weight ratio of zirconyl chloride salt to polyvinylpyrrolidone (PVP) polymer in liquid precursors was investigated for its effect on the spinnability and formation of precursor fibers as well as on the resulting fibrous ZrO_2. The precursor fiber generation measured at a rate up to 5.6 g/h was achieved with a single flat 25-mm diameter alternating current (AC) electrode, which corresponded to production of up to 1.5 g/h of fibrous ZrO_2. The calcination process involved annealing the fibers at temperatures which ranged from 600 ^{o}C to 1000 ^{o}C and produced 0.1–0.2 mm thick fibrous ZrO_2 meshes. Individual nanofibers were found to have diameters between 50–350 nm and either a tetragonal (t-ZrO_2) or monoclinic (t-ZrO_2) structure depending on the calcination temperature. The annealed meshes with total porosity between 98.0±0.2% and 94.6±0.2% showed little deformation or cracking. Tensile strength and modulus of fibrous t-ZrO_2 meshes strongly depended on porosity and varied from 0.07±0.03 MPa to 1.05±0.3 MPa and from 90±40 MPa to 388±20 MPa, respectively. The m-ZrO_2 meshes resulted similar moduli, but much lower strengths due to their brittleness. A power-law relationship between the elastic modulus and porosity of AFES-derived nanofibrous t-ZrO_2 meshes, in comparison with other porous zirconia materials, was also investigated. The results of this study have demonstrated the feasibility of free-surface AFES in sizeable production of zirconia nanofibers and highly porous nanofibrous ceramic structures.

Keywords: **A**. Fibres; **B**. Mechanical Properties; **C**. ZrO_2; **D.** Electrospinning.

1. Introduction

Zirconium dioxide (ZrO_2) fibers with sub-micrometer to sub-100 nm diameters have been demonstrated as a promising material for improving the efficiency and performance of many material systems and device structures. This material can be used for a range of applications including, but not limited to, a separator in solid oxide fuel cell [1], a support catalyst in a chemical reaction [2,3], a filtration membrane [4], an absorber [5], as well as a scaffold for tissue regeneration [6].

In most situations, such ZrO_2 fibers and fibrous assemblies have been made by thermal treatment of polymer-based precursor fibers prepared by the electrospinning method [7-18]. In the early reports on the subject, Shao et al [12] prepared ZrO_2 nanofibers with 50–200 nm diameters and single phase monoclinic crystalline structure by calcination of the electrospun 0.5:1.0 weight ratio $ZrOCl_3$/polyvinyl alcohol (PVA) precursor fibers at 800 ^oC. Jing et al [13] found that ZrO_2 nanofibers with the diameters as small as 13–40 nm can be produced from electrospun polyvinylpyrrolidone (PVP)-based precursors. Later, many combinations of zirconium compounds (zirconyl chloride octahydrate, zirconium acetate, zirconium n-propoxide and butoxide) or ZrO_2 nanoparticles with polymers (PVA, PVP, polyethylene oxide (PEO), polyvinylacetate (PVAc)) were successfully electrospun and converted to zirconia fibers with either tetragonal (t-ZrO_2) or monoclinic (m-ZrO_2) structures. For example, Zhao et al [11] used a water-ethanol solution of zirconyl chloride ($ZrOCl_2$) octahydrate and PVP to prepare the precursor fibers with ~200 nm diameters by using a capillary needle DC-electrospinning technique. Zirconia nanofibers with 80–150 nm diameters were crystallized from the precursor fibers by annealing at 400–800 ^oC in air. Nanocrystalline t-ZrO_2 phase formed during the calcination between 400 and 600 ^oC, and it was fully transformed to m-ZrO_2 phase at 800 ^oC.

Similar calcination behavior was observed by Davies et al [14] who observed that $ZrOCl_2$/PVP (10:1 weight ratio) precursor fibers with diameters which ranged from 1200 to 800 nm converted to *m*-ZrO_2 phase at temperatures above 750°C. In another example, Singh et al [15] found that both tetragonal and monoclinic phases co-exist in ZrO_2 nanofibers after the calcination of zirconium n-propoxide/PVA precursor fibers at 800 ^{o}C, whereas a pure monoclinic phase was obtained at 1050 ^{o}C without noticeable changes in the fibers' shape and morphology. Saligheh et al [16] prepared zirconia nanofibers from electrospun zirconium acetate/PVA precursors and observed their gradual transition from tetragonal and monoclinic ZrO_2 structure after the calcination between 500°C and 1100°C. Here, it was noted that *t*-ZrO_2 phase fully disappears around 1100 ^{o}C and the resulting grain size of *m*-ZrO_2 phase was close to the fiber diameter. Li et al [17] found similar crystallization behavior of zirconia fibers from the electrospun 5–10 nm amorphous zirconia particles/PVP precursor. In that case, the crystallization of *t*-ZrO_2 phase started at 450 °C, began to transform to *m*-ZrO_2 phase at 650 °C, and showed a single monoclinic phase at 1000 ^{o}C. Rodaev et al [18] reported that the amount of *m*-ZrO_2 phase formed during the calcination of $ZrOCl_2$/PEO precursor fibers at 800 ^{o}C depending on the corresponding salt/polymer weight ratio. Changing the weight ratio from 1.0:1.0 to 4.0:1.0 resulted in progressively higher content of monoclinic phase (from ~10 to 87 vol%) [18].

It can be summarized that the type and relative amounts of the zirconium compound and polymer, together with specifics of their interaction and decomposition in precursor fibers, influence the crystallization process and textural properties of the resulting zirconia fibers. Regardless of the source of zirconia and nature of polymer in the electrospun precursor fibers, the nanocrystalline *t*-ZrO_2 phase usually forms first during the decomposition of precursors. The presence of *t*-ZrO_2 phase in zirconia nanofibers is explained by Garvie's theory [19], which relates the occurrence of tetragonal phase to the stabilizing effect of excess surface energy which is associated with a small (< 30 nm) characteristic size of crystallites. Some recent findings, on the other hand, indicate that the formation of *t*-ZrO_2 phase could be due to either the chemical reactions during the decomposition of intermediate compounds, the presence of various types of impurities, and/or oxygen deficiency [20]. Gradual conversion of initially formed *t*-ZrO_2 to *m*-ZrO_2 occurs as the polymeric residue burns out and the growth of crystallites destabilizes the initial phase [21,22].

In many experiments on the preparation of nanofibrous zirconia from electrospun precursors, suitable stabilizing additives have been used to prevent the formation of *m*-ZrO_2 [23-26]. The presence of such additives generate a crystalline field that promotes the formation of *t*-ZrO_2 over *m*-ZrO_2 [21,22]. For example, Castkova et al [27] prepared yttria-stabilized zirconia (YSZ) fibers from electrospun zirconium n-propoxide/PVP precursors with yttrium nitrate or chloride as a dopant. Thin nanofibrous (100–250 nm diameter) YSZ meshes were found to be rather flexible after the calcination at 700 ^{o}C, but became very brittle after the calcination at 1100 ^{o}C. Gazquez et al [6] used a similar precursor to prepare flexible YSZ nanofibrous meshes with 530 ± 120 nm fiber diameters and 0.12 mm fibrous mat thickness at 850 ^{o}C. Bending tests performed on both nanofibrous meshes and individual fibers revealed the Young's moduli of 1.1± 0.24 MPa and 30± 3 GPa, respectively [6]. Mao et al [4,28] indicated that the strength and Young's modulus of 800 ^{o}C calcined YSZ fibrous meshes can depend on the fiber diameter and mesh density. The best values achieved during tensile tests were 540 MPa Young's modulus and 5 MPa strength for the densest nanofibrous YSZ meshes with fiber diameters ~280 nm.

In almost all studies on the formation of fibrous zirconia, the precursor fibers were prepared by a capillary needle DC-electrospinning technique, which is a very slow process. The precursor fibers are normally collected on an electrically grounded metal collector where they can remain electrically charged when a fibrous layer is formed. These factors influence the fiber arrangement and interaction within the layer, which can affect the behavior of fibrous assembly during thermal treatment as well as the resulting properties of nanofibrous structures. Although the mechanical properties of ceramic nanofibers are critical for many applications, the available data on zirconia nano- and sub-micrometer fibers is limited to only few studies which were cited above on YSZ fibrous meshes.

The current work presents the first results on the crystallization and corresponding mechanical properties of undoped, nanofibrous zirconia which was derived from fibrous precursor material prepared by free-surface alternating field electrospinning (AFES). This electrospinning technique produced a dense, slow moving fibrous flow where the propagating fibers carried little to no electric charge [29]. Together with a high rate of fiber generation, this process allowed more flexibility in the collection and handling of nanofibers. Up until now, AFES has been only utilized with a few types of polymers [30,31] and alumina ceramic [32] precursors. The presented data demonstrate the feasibility of sizeable production of highly porous nanofibrous zirconia meshes with good mechanical integrity from AFES precursor fibers based on zirconyl chloride and PVP.

2. Materials and Methods

2.1 Precursor materials

Zirconyl chloride ($ZrOCl_2$) octahydrate (98+%, Alfa Aesar), polyvinylpyrrolidone (PVP, M_w 1,300,000, Alfa Aesar), N, N-Dimethylformamide (Reagent grade, Fisher Chemical) and ethanol (200 Proof, Fisher BioReagents) were used to prepare the precursor solutions for electrospinning. The salt and polymer were dissolved in DMF and ethanol, respectively, and the solutions were mixed to obtain the salt-to-polymer weight ratios in a range from 1.5:1.0 to 2.5:1.0 in a base precursor with 10 wt% of polymer. The base precursor was then diluted to desired polymer concentration with a DMF/ethanol mixture to maintain the 1:1 DMF/Ethanol weight ratio. The precursors were stirred for up to 24 h using a magnetic stirrer and stored at normal laboratory conditions. The precursors were stable for at least one month.

2.2. Precursor solution analysis

Viscosity of $ZrOCl_2$/PVP precursor solutions was determined using a HAAKE RotoVisco 1 (Thermo Scientific) viscometer in a parallel plate configuration and Rheowin 4 Job and Data Manager Software. The viscometer was calibrated prior to each test and between 0.2 and 3.0 mL of precursor, depending on the apparent viscosity, was used per test. All tests were performed in triplicate at 20º C. Apparent viscosity as a function of time was measured at steady shear rate of 1000 rpm over a period of 120-seconds. The recorded viscosity values were stored within the Rheowin 4 Data Manager and later exported for further analysis.

Electrical conductivity of the precursor solutions was measured using the WTW inoLab pH/Cond 720 instrument (WTW-Xylem Analytics, Weilheim, Germany). The meter was calibrated according to the WTW inoLab 720 instruction manual. The AutoRead function was used to obtain at least 5 stabilized values for each sample. These values were recorded for further analysis.

2.3. Fabrication of fibrous meshes

Generation of $ZrOCl_2$/PVP precursor nanofibers was done by using an alternating field electrospinning (AFES) system capable of producing AC-voltages up to 40 kV rms and operated at 60 Hz [31,32]. Liquid precursor solution was loaded in an electrically insulated fluid line equipped with a pump and delivered at up to 40 mL/h through the base of the fiber-generating electrode. Electrodes with flat surfaces and diameters ranging from 10 to 40 mm were used during experimentation. Generated fibers were collected on a rotating plastic cylinder with 10 cm diameter which was placed at 20–25 cm above the fiber-generating electrode. The formation of a stable flow of fibers and the uniformity of formed fibrous meshes served as major criteria for the selection of precursors and process parameters for further experiments. The generation of fibrous flows was recorded at up to 1/12500 s exposures (still photos) using a Sony DSC-RX10M2 camera. The collected nanofibrous sheets had lateral dimensions usually around 30 cm × 20 cm and thicknesses ranging from 0.3 to 0.5 mm. The meshes were then removed from the support and dried in an oven at 120 ^{o}C to eliminate the residual solvent and stabilize the material. Next, the fibrous $ZrOCl_2$/PVP sheets were cut in smaller pieces and placed between the porous ceramic plates in a programmable furnace (Isotemp from Fisher Scientific). The fibrous sheets were then heated at a rate up to 10 ^{o}C/min and calcined in air or argon at temperatures ranging from 600 ^{o}C to 1000 ^{o}C for 2 hours.

2.4. Characterization

Thermogravimetric Analysis (TGA) analysis included simultaneous recordings of thermogravimetric (TG), differential thermal analysis (DTA) and differential thermogravimetric (DTG) curves, and it was performed using TG/DTA-SETSYS-16/18 (SETARAM, France) instrument coupled through a heated capillary adapter to a quadrupole mass spectrometer (QMS-

422 ThermoStar from Balzers Instruments, 100 amu, 70 eV electron impact ionization) to monitor principal volatile species produced during the pyrolysis of $ZrOCl_2$/PVP precursor fibers. The samples were placed into the alumina crucibles and the mass of the samples varied between 7 and 12 mg. The TGA–DTA and MS spectra were recorded in air (flow rate 50 mL/min) at temperatures ranging from 20 to 900 ^{o}C with heating rate of 10 ^{o}C/min. MS data was processed using the Quadstar 422 software.

FTIR spectra (Vertex 70 spectrometer, Bruker Optics) of the as-prepared and calcined precursor fibers were recorded in transmission mode. FTIR spectra represented an average of 32 scans recorded with a resolution of 4 cm^{-1} for each sample. As-prepared precursor fibers were dried at 120 ^{o}C to remove the solvent before taking the measurements.

The size, shape, and surface morphology of calcined ZrO_2 nanofibers was determined using the field-emission scanning electron microscopy (FE-SEM, FEI Quanta 650). The samples were sputter coated with a few nanometers of Au-Pd to reduce the charging. SEM imaging was done in a secondary electron mode at an accelerating voltage of 15 kV, an electron probe current of 2 μA, and a chamber pressure of 1×10^{-4} Pa. SEM images were analyzed using ImageJ program to estimate the fiber diameters as well as the grain sizes for the samples which had been calcined at 1000 ^{o}C.

A PANalytical X'Pert Pro MPD diffractometer (Cu Kα tube operated at 40 kV and 45mA, PANalytical X'Celerator detector, the Bragg–Brentano geometry) was employed to obtain X-ray diffraction (XRD) patterns of nanofibrous ZrO_2. Data was acquired over the range of 5–90° 2θ using the step of 0.0167° and dwelling time of 27 seconds. Samples were rotated during the measurements to minimize the possibility of preferred orientation effects. Phase identification and crystallite size analysis were performed using the PANalytical High Score Plus software package and the International Centre for Diffraction Data (ICDD) powder diffraction file (PDF-2 ver. 2009) database.

The tensile moduli and strength of the nanofibrous ZrO_2 meshes were determined using ADMET eXpert 4000 microtester (ADMET Inc., Norwood, MA, USA) equipped with either 0.5 N or 5 N load cells and MTESTQuattro controller. The specimens with the 2–6 mm width and gauge length of 10 mm were tested at 0.05 mm/s loading rate. The data was corrected for the load cell deflection and initial position of the stage. At least five test samples were cut from the exact same nanofibrous ZrO_2 sheet to be analyzed. The long side of each sample corresponded to the direction of fiber collection during the electrospinning process. The dimensions and mass of each sample were determined individually using a digital micrometer, caliper and precision balance. Porosity of nanofibrous ZrO_2 meshes was estimated according to formula 1 below.

$$\varepsilon = (1 - \rho_{\mathrm{exp}}/\rho_{\mathrm{zirconia}})\times 100\%, \quad (1)$$

where ρ_{exp} is the bulk density of the sheet and $\rho_{\mathrm{zirconia}} = 6.10$ g/cm^3 for t-ZrO_2 and 5.83 g/cm^3 for m-ZrO_2 phases, respectively [33].

The flexural modulus of the thin nanofibrous zirconia sheets was determined using their deflection δ when the sheet was clamped on one end according to formula 2,

$$\delta = wL^4/8EI_c, \quad (2)$$

where w is the weight of the sample, L is the length, and E is the flexural modulus, and centroidal moment of inertia of the cross section is determined using formula 3 below,

$$I_c = bh^3/12, \quad (3)$$

where b is the width, h is the thickness of the nanofibrous sheet.

3. Results and discussion

3.1. Precursor properties

Viscosity and electrical conductivity of the precursor solution play critical roles in electrospinning. AFES process appears to be even more sensitive to these parameters than DC-electrospinning. In a case of $ZrOCl_2$/PVP precursor, the best spinnability in AFES process was achieved with the polymer concentrations between 6 and 8 wt%. Those precursors had the apparent viscosity of the solution in the range of 80–160 mPa.s and electrical conductivity in the range of 2.5–8 mS/m (**Fig.1**). The increase in concentration of zirconyl chloride led initially to higher values of both viscosity and conductivity of the precursor followed by the saturation of these parameters, depending on the polymer concentration and salt/PVP weight ratio. Such behavior is determined, to some extent, by the nature of interaction between the salt and polymer molecules [34,35]. It was also noted that the as-spun fibrous sheets from 2.5:1 $ZrOCl_2$/PVP precursor appeared rather wet at such salt/polymer ratio due to hygroscopicity of the salt even when 6 wt% precursors were used. As a result, the fibers were noticeably fused in as-spun fibrous material because of the increased amount of residual solvent and water during the fast accumulation of precursor fibers on the collector. The precursors became too viscous for AFES process at the PVP concentration of 9 wt% and above, whereas at lower than 6 wt% PVP concentration the fiber generation became intermittent and partial electrospraying occurred.

3.2. Electrospinning and calcination of fibrous meshes

When operated within the precursor spinnability range, AFES was capable of producing a stable flow of precursor fibers in a broad range of AC-voltages (**Fig.2**). Some fiber generation was observed at voltages as low as 7.5 kV rms, which is near the corona inception voltage threshold [36]. Voltages below this threshold do not result in the ionic wind phenomenon which is the force that drives the flow upward. The best productivity was achieved at AC-voltages within the range of 20–27 kV rms (Fig.2c,d), depending on the precursor. For example, when using the electrode with the 25 mm diameter the yield of $ZrOCl_2$/PVP precursor fibers was between 3.0 and 5.6 g/h, which, after annealing, corresponded to productivity of 0.7–1.5 g/h of nanofibrous zirconia. Although higher fiber generation rates can be achieved at higher voltages, the fibers spread too much to be efficiently collected (Fig.2e). Besides, the propagating fibers tend to self-assemble into the strands as seen in the top areas of the propagating flows in Fig.2b-e. The formation of fibrous strands was less noticeable when the collecting surface was positioned at 15.0–22.5 cm from the fiber-generating electrode. In a typical process, the fibrous flow was found to move toward the collector with the speed of 0.9–1.1 m/s. The $ZrOCl_2$/PVP precursor fibers were assembled into the fibrous sheets on the collector surface by matching its speed to that of the fibrous flow (Fig.2a). This resulted in the $ZrOCl_2$/PVP precursor fibrous sheets (Fig.2f) with partial alignment of microscopic strands of fibers along the direction of collection (Fig.2f, inset). Thermal treatment of precursor fibrous sheets at temperatures up to 1000 ^{o}C resulted in up to 2.5±0.3 times linear shrinkage of the material. The resulting nanofibrous ZrO_2 sheets showed little deformation and surface morphology resembling the original sheet (Fig.2g,h).

3.3. Thermal processing of precursor fibers

FTIR analysis of as prepared and dried (80 ^{o}C) $ZrOCl_2$/PVP precursor fibers (**Fig.3**) indicates the appearance of the absorption bands at 1585 and 1021 cm^{-1} that are absent in pure PVP fibers. These bands increase in intensity proportionally to the amount of the salt content in the precursor fibers and they are attributed to –OH bending and deformation modes in zirconyl chloride tetrahydrate, respectively [37]. Other bands were associated with PVP and most of them shift or change in intensity, proportionally to the increase of the amount of salt in precursor fibers, due to possible formation of complexes [38].

Regardless to $ZrOCl_2$/PVP mass ratio in the precursor fibers, the FTIR spectra of fibers calcined at 600 ^oC (Fig.3b) show almost no features except a weak band at 570 cm^{-1}. Well-defined 482 and 569 cm^{-1} absorption bands appear after the calcination at 800 ^oC, whereas a small peak appears at 450 cm^{-1} and broad absorption band intensifies between 620 and 800 cm^{-1} after a 1000 ^oC process. These results resemble the evolution of infrared spectra of pure zirconia nanoparticles when their size increases from 10 to 50 nm and the phase composition changes from primarily tetragonal to monoclinic during the calcination [39,40]. Calcined nanofibrous sheets maintained the original arrangement of fibers in as-spun material, both at macro- and microscale (Fig.3b, inset).

Thermal Gravimetric Analysis (TGA) of the precursor fibers with different $ZrOCl_2$/PVP mass ratios (1.5:1.0, 2.0:1.0 and 2.5:1.0) was performed to determine the procedure for thermal treatment. TG curves of the precursor fibers with different $ZrOCl_2$/PVP weight ratios indicate two distinct regions of mass loss regardless of the $ZrOCl_2$/PVP mass ratio (**Fig.4**). The first region (70–150 ^oC) is where the zirconyl chloride octahydrate loses most of its water [37]. Salt dehydration continues slowly as temperature increases and further decomposition of the salt and polymer components occur between 300–550 ^oC. SIMS analysis of the effluent gases indicated the emission of CO_2 as the main component in this range of temperatures. Main stage of $ZrOCl_2$ decomposition occurs between 330 and 380 ^oC with increased emission of CH_3Cl, HCl, and oxychlorine species observed in the secondary ion-mass spectra [41]. This follows the observations that zirconium oxide phase starts to form around 400 ^oC [27,42]. The emission of

HC=CH and HC–CH_2 species from the vinyl group of PVP peaks up at 350 and 450 °C, whereas the emission of NO and other species associated with the decomposition of the pyrrolidone ring peak up at 350, 450, and 520 °C. The apparent maxima in DTA and DTG curves corresponded to changes in the emission of mentioned gaseous components. The mass reduces only by 1.0–2.0 % between 550 and 850 °C and it is associated mainly with removal of the residual carbon.

The shrinkage of the $ZrOCl_2$/PVP precursor fibrous sheets was proportional to their mass loss behavior. The linear shrinkage of the material is only 3% at temperatures below 200 °C, but shrinks another 50–55% between 300 and 550 °C. The TGA and shrinkage behavior data were used to choose the thermal treatment procedure for the ZrO_2 fiber crystallization from free-standing $ZrOCl_2$/PVP precursor fibrous sheets. The procedure included temperature ramping at 2 °C/min to critical temperatures (100, 220, 330, 450 and 550 °C) with holding at each temperature for 0.5 h, followed by heating at 3 to 7 °C/min rate to the final temperature (600, 800, or 1000 °C) and holding at that temperature for 2 h. This resulted in the ZrO_2 nanofibrous meshes with a little deformation and lack of cracking (Fig.2g,h).

Average diameters of ZrO_2 nanofibers crystallized at 600 °C and 1000 °C from the precursor fibers with different $ZrOCl_2$/PVP weight ratios vary in the range from 70 to 230 nm (**Fig.5**). Bundled and fused fibers that appear as single fibers were excluded from the determination of the fiber diameters and their size distributions. The observed trends correlate with the viscosity of the precursors (Fig.1b) and the relative amount of salt. For example, the precursors with higher viscosity tend to produce the fibers with larger diameters. Smaller diameter of ZrO_2 fibers crystallized from 2.5:1 weight ratio $ZrOCl_2$/PVP precursor can be explained by a combination of saturated viscosity numbers and increased electrical conductivity of the precursor solution. This could lead to the generation of thinner liquid jets during the AFES process and, consequently, the thinner fibers. The fibers in fibrous sheets prepared from the 8 w% precursor solution with 2.5:1 weight ratio of $ZrOCl_2$/PVP were too fused to reliably determine their diameters. It was also noted that ZrO_2 fibers crystallized from 1.5:1 weight ratio $ZrOCl_2$/PVP precursor had a narrower size distribution and are truly nanofibers with average diameters less than 100 nm when prepared from the 6 w% precursor solution (Fig.5, insets). There was relatively small variation in ZrO_2 fiber diameters and their size distribution after calcination at different temperatures for all tested $ZrOCl_2$/PVP weight ratios.

3.4. Microstructure and phase composition of calcined zirconia nanofibers

Some representative SEM images of the ZrO_2 fibrous sheets calcined at 600 ^{o}C are shown in **Fig.6**. The fiber diameters as well as the degree of fiber bundling and fusion increased when the materials were prepared from precursors with larger $ZrOCl_2$/PVP weight ratios (Fig.6c). The same trend was observed for higher precursor concentrations. It was also noted that the more fused $ZrOCl_2$/PVP precursor fibrous sheets resulted in mechanically weak ZrO_2 fibrous structures that break easily after the calcination.

There were little changes in the microarchitecture of ZrO_2 fibrous sheets which were calcined at 1000 ^{o}C (**Fig.7**) except the noticeable ZrO_2 grain growth (Fig.7d-f). Yet, there was little breakage of individual fibers observed even in the nanofibers with diameters comparable to apparent grain size in the range of 40–100 nm (a few such nanofibers are highlighted in Fig.7d and Fig.7f).

XRD analysis (**Fig.8**) of ZrO_2 fibers prepared from the $ZrOCl_2$/PVP precursor fibers with different salt/polymer weight ratios showed that, after the calcination at 600 ^{o}C (Fig.8a), the materials are composed mainly of a nanocrystalline tetragonal phase of zirconia (t-ZrO_2). The calculated average crystallite sizes of t-ZrO_2 phase were 11.7 nm, 8.4 nm, and 8.3 nm when prepared from precursors with 1.5:1, 2.0:1, and 2.5:1 weight ratios, respectively. The decrease of crystallite size with the increasing salt/polymer weight ratio can be related to restricted diffusion due to the fast nucleation rate of zirconia clusters and formation of amorphous zirconia gel during the initial stage of heat treatment below 300 °C (Fig.4b). It is possible that, at 1.5:1 $ZrOCl_2$/PVP weight ratio, more isolated and larger amorphous zirconia particles form. This results in larger t-ZrO_2 crystallite sizes at 600 °C and creates local conditions favorable for partial conversion of t-ZrO_2 to m-ZrO_2 at that temperature. The tetragonal phase undergoes gradual transition to monoclinic phase as the crystallite size increases in all samples at higher temperatures (Fig.8b,c). It can be also seen that the fibers prepared from 1.5:1 $ZrOCl_2$/PVP precursor convert faster to monoclinic phase. According to formulas for the tetragonal (C_m) and monoclinic (C_m) phase content [43]:

$$C_t = I_{(111)t} / [I_{(111)t} + I_{(111)m} + I_{(11\text{-}1)m}], \text{ and } C_m = 1 - C_t, \quad (4)$$

where $I_{(hkl)}$ are the integral peak intensities of corresponding phases, the amount of m-ZrO_2 phase in 600 °C-calcined fibers from 1.5:1 $ZrOCl_2$/PVP precursor was 14±3 %. After the calcination at 800 °C, the amounts of m-ZrO_2 phase in fibers prepared from 1.5:1, 2.0:1 and 2.5:1 $ZrOCl_2$/PVP precursors was 79±3, 59±3, and 62±3 %, respectively. The calculated average crystallite size reached 38±5 nm in all samples after the calcination at 800 °C and further crystal growth up to 58±10 nm was observed at 1000 °C. It was also noted that for both 800 and 1000 °C calcination temperatures the calculated crystallite size was statistically a few nm smaller in zirconia nanofibers prepared from the precursors with higher ratio of salt to polymer. The calculated average crystallite sizes are within the range of zirconia grain dimensions estimated from SEM images (Fig.7d-f).

There are few reports on the effect of salt/polymer weight ratio on the crystallization of pure zirconia fibers. Rodaev et al [18] found that 800 ^{o}C calcination of $ZrOCl_2$/PEO fibers yields more *m*-ZrO_2 phase when salt/polymer ration is higher. This seems to oppose the present results, but the explanation can be simple. It has been shown that the transition of *t*-ZrO_2 to *m*-ZrO_2 occurs when a critical size of the crystallite is reached [19,44]. This is the case in both the present study and in article cited above [18]. However, the growth of crystallites can be affected by several factors, including the salt/polymer weight ratio in the precursor fiber, interaction between the zirconia precursor and polymer matrix, polymer's degradation behavior, and thermal processing procedure. For example, Yin et al [45] found that annealing of $ZrOCl_2$/PVP/PAN precursor fibers in air and N_2 at 900 ^{o}C resulted in less *m*-ZrO_2 phase when the carbonaceous matrix is retained after the annealing in non-oxidizing atmosphere.

To clarify the issue further, **Fig.9** compares the XRD patterns of ZrO_2 nanofibers prepared in present study at different heating rates and atmospheres from AFES precursor fibers with 1.5:1 $ZrOCl_2$/PVP weight ratio. Higher heating rate resulted in significantly larger fraction of *t*-ZrO_2 phase remaining in the material after calcination at 800 ^{o}C. It can be logically assumed that faster heating leads to faster nucleation of small zirconia crystallites and leaves more carbonized polymer residue upon reaching the desired calcination temperature. Such residue can restrict the surface diffusion and crystal growth. Almost the same amount of *t*-ZrO_2 phase remained in nanofibrous zirconia even after calcination at 1000 ^{o}C when the thermal processing occurred under argon. These results fit crystallite size and impurity theories [19,20] and confirm the role of carbonized residue and thermal processing procedure in the crystallization of nanofibrous zirconia from electrospun precursors.

Furthermore, more detailed analysis of TG curves (Fig.4a) indicates that there still about 1% of mass loss in the 1.5:1 fibers annealed between 550 ^{o}C and 770 ^{o}C at 10 ^{o}C/min. There was no mass change observed above 770 ^{o}C. Both the 2.0:1 and 2.5:1 fibers lost about 2% of mass between 550 and 880 ^{o}C, thus some carbon residue can still be present in these materials upon reaching 800 ^{o}C. Such mass losses could correspond roughly to removal of 1.0–2.0 nm thick carbon layer that can still be present on the surface of 8–12 nm t-ZrO_2 crystallites at 600 ^{o}C. As a result, t-ZrO_2 to m-ZrO_2 phase transformation would take longer if not all carbon residue is removed before reaching the desired calcination temperature.

3.5. Mechanical properties of nanofibrous zirconia meshes

Fibrous meshes prepared from 2.0:1 weight ratio $ZrOCl_2$/PVP fibers electrospun from a 7 wt% liquid precursor demonstrated the best thickness uniformity and smallest deformation during thermal processing. Several such fibrous meshes were prepared from precursor fibers obtained at different AC-voltages (20–27 kV RMS) and speed of collecting surface (0.9–1.1 m/s to match the speed of the fibrous flow). The resulting ZrO_2 fibrous meshes had lateral dimensions up to 100 mm × 70 mm and thicknesses in the range of 0.1–0.2 mm after the calcination between 600 and 1000 ^{o}C. They were highly porous (between 94.3 and 98.2 %), but exhibited reasonable mechanical integrity (Fig.2g,h) which allowed to conduct initial evaluation of some samples in tension and bending. Tensile strength and modulus of t-ZrO_2 fibrous samples increased from 0.07±0.03 MPa to 1.05±0.3 MPa and from 90±40 MPa to 388±20 MPa, respectively, when the porosity reduced from 98.0±0.2% to 94.6±0.2%. **Fig.10** shows several exemplary strain-stress curves of t-ZrO_2 and m-ZrO_2 meshes in tension. The m-ZrO_2 sample with 96.5% porosity showed similar magnitude of strength (0.25–0.37 MPa) as the t-ZrO_2 sample with

97% porosity, but much larger modulus due to, perhaps, higher intrinsic stress in a partially bundled fibrous network. The results for *m*-ZrO_2 samples were strongly affected by slippage due to the local cracking and separation of fiber fragments at the contact surface between the sample and device grips. Because of high brittleness of samples calcined at 1000 ^{o}C, it was not possible to obtain reliable data for *m*-ZrO_2 fibrous meshes with other porosities in these experiments. The tensile behavior of the *t*-ZrO_2 sample with 97% and higher porosity resembles that of elastomers. This result can be due to high deformability of individual zirconia nanofibers and fiber bundles as well as relatively insignificant fiber-fiber interaction at this porosity. At lower porosities, the fiber-fiber interaction increases and more fused contact points form between the fibers. This increases the rigidity of fibrous network and results in the stress-strain curves more typical for brittle structures. The *t*-ZrO_2 fibrous meshes with 94.6±0.2% porosity revealed the tensile strength between 0.75 and 1.35 MPa.

Fig.11 summarizes the experimental data for tensile moduli of *t*-ZrO_2 and *m*-ZrO_2 fibrous samples (Fig.11c,d). These results are compared with several data points for the flexural moduli determined in a one-end clamped cantilever test for the samples calcined at 600 and 1000 ^{o}C (Fig. 11a,b). The trend in experimental data (*t*-ZrO_2 only) was compared to a simple power law relationship between the tensile modulus and density in porous and cellular materials according to [46-48]:

$$E_{\mathrm{porous}}/E_{\mathrm{solid}} = C(\rho_{\mathrm{porous}}/\rho_{\mathrm{solid}})^{n}, \quad (5)$$

where E_{porous}, E_{solid} and ρ_{porous}, ρ_{solid} are the moduli and density for porous and non-porous state of the material, respectively. The parameter C is a dimensionless constant frequently selected as ~1.0, and the exponent n varies depending on the cell morphology (frequently chosen as n=2 for open cell and n=3 for closed cell structures, respectively).

It can be seen that the experimental data for *m*-ZrO_2 meshes with 96.5% porosity match the relationship (5) at n=2, although, the lack of other data points for this test does not allow the establishment of a trend. The results for *t*-ZrO_2 fibrous meshes (Fig.11d) fit between the curves for *n=2 and n=3*, but the trend cannot be fitted by using the relationship (5). Published data for various zirconia ceramics with porosity less than 55 % [49-56] show reasonable fit at n=3 (Fig.10e) in this model. It was necessary to note that this, and a number of other similar models [52], have been applied mostly to fit the experimental data in a narrow range of porosities. In this case, it was assumed that the prepared highly-porous nanofibrous zirconia samples could be treated as mostly open-cell cellular solid with the cell and cell edge structure being different from those in referenced ceramic materials. The fiber bundling, deformation, degree of local alignment, and interaction along and across the fibers create a complex network with properties that can strongly depend on the overall density of a fibrous mat. Therefore, in a fibrous ceramic structures, the exponent n can vary as the total porosity changes. In addition, the elastic modulus of individual zirconia fibers may differ from that in solid material [6] due to the fibers' microporosity, grain size and diameter. The relationship (5) has, therefore, been modified to fit the experimental data in the entire range of porosities:

$$E_{exp} = E_t(1 - C_1\varepsilon^m)(1 - C\varepsilon)^n \quad \text{where } n = (C_2 - C_3\varepsilon^k) \qquad (6)$$

In this expression, the empirical parameters C_1 and m are associated with the possibility that the modulus of the cell walls (edges) can change depending on their structure. Their magnitudes, in this case, were set under the assumption that the Young's modulus of individual *t*-ZrO_2 nanofibers is indeed 30±3 GPa according to Gazquez et al [6]. Parameters C_2, C_3 and k are associated with the changes in the type (open or closed), geometry and elastic response of the cell [57] depending on the total porosity. For example, the best-fitting curve in Fig.11e has been obtained for E_t = 219 GPa (bulk t-ZrO_2) [58], C_1=0.965, m=2.7, C_2=3.0, C_3=1.74, and k=3.4. The magnitude of C_2=3 reflects the initially closed cell type at low porosity, whereas C_3 and k are the parameters that reflect the changes in the cell's microarchitecture and properties.

These preliminary results show that, in nanofibrous zirconia meshes prepared from AFES precursor fibers, the resulting process-specific microarchitecture of the fibrous network can strongly affect the mechanical properties of the assembly.

4. CONCLUSIONS

Free-surface high-yield alternating field electrospinning (AFES) process has been developed in this work to prepare up to 5.6 g/h of fibrous zirconia precursor material based on zirconyl chloride and PVP polymer. The specifics of ionic wind driven fibrous flow and flow speed-matched fiber collection resulted in good thickness uniformity over a 20-cm width of the fibrous zirconia precursor meshes. It is anticipated that this process can be relatively easily scaled up for increased productivity. Thermal treatment of the precursor fibers at the calcination temperatures up to 1000 ^{o}C resulted in free-standing pure zirconia meshes with average fiber diameters in a range of 70–230 nm. Despite significant shrinkage of the material, the fabricated ZrO_2 nanofibrous meshes showed small deformation and little cracking. It has been shown that the carbon residue from the decomposed polymer matrix influence the formation of the crystalline structure and phase composition of zirconia fibers at given calcination temperature, depending on the weight ratio of salt to polymer in the precursor. Further optimization of AFES precursor composition as well as fiber collecting and the corresponding thermal processing procedures is expected to improve the uniformity and mechanical properties of the resulting nanofibrous zirconia meshes. Preliminary data of mechanical tests indicated a possible effect of the fiber structure, arrangement, and interaction in AFES-derived zirconia meshes on the relationship between their elastic modulus, strength, and porosity. Further studies will be directed towards a better understanding of the correlation between mechanical properties of porous nanofibrous ceramics and their corresponding microarchitectures.

ACKNOWLEDGEMENTS

This work has been supported by the National Science Foundation (NSF) [Grant number DMR-1708600]. Riley Yager thanks the support from the NSF International Research Experience for Students (IRES) Program [Grant number OISE-1558268] and from the EU Erasmus+ Program.

REFERENCES

1. J.Y.Koo, Y. Lim, T.B. Kim, D. Byun, W. Lee, Electrospun yttria-stabilized zirconia nanofibers for low-temperature solid oxide fuel cells, Int. J. Hydrogen Energy. 42 (2017) 15903–15907. https://doi.org/10.1016/j.ijhydene.2017.04.099
2. C. Lee, Y.G. Shul, H. Einaga, Silver and manganese oxide catalysts supported on mesoporous ZrO_2 nanofiber mats for catalytic removal of benzene and diesel soot, Catal. Today. 281 (2017) 460–466. https://doi.org/10.1016/j.cattod.2016.05.050
3. E. Formo, M.S. Yavuz, E.P. Lee, L Lane, Y. Xia, Functionalization of electrospun ceramic nanofibre membranes with noble-metal nanostructures for catalytic applications, J. Mater. Chem. 19 (2009) 3878–3882.

https://doi.org/10.1039/b901509d

4. X. Mao, Y. Bai, J. Yu, B. Ding, Flexible and highly temperature resistant polynanocrystalline zirconia nanofibrous membranes designed for air filtration, J. Am. Ceram. Soc., 99 (2016) 2760–2768.

   https://doi.org/10.1111/jace.14278

5. Y. Tang, Z. Liu, K. Zhao, S. Fu, S. Adsorption and separation properties of positively charged ZrO_2 nanofibrous membranes fabricated by electrospinning, RSC Adv. 7 (2017) 42505–42512.

   https://doi.org/10.1039/c7ra08227d

6. G.C. Gazquez, H. Chen, S.A. Veldhuis, A. Solmaz, C. Mota, B.A. Boukamp, C.A. van Blitterswijk, J.E. ten Elshof, L. Moroni, Flexible yttrium-stabilized zirconia nanofibers offer bioactive cues for osteogenic differentiation of human mesenchymal stromal cells, ACS Nano 10 (2016) 5789–5799.

   https://doi.org/10.1021/acsnano.5b08005

7. Z. Liu, M. Fang, C. Tang, M. Wang, Y. Mao, Z. Huang, Y. Liu, X. Wu, Preparation and characterization of ZrO_2 nanofibers and nanobelts by electrospinning, Key Eng. Mater. 697 (2016) 701–705.

   https://doi.org/10.4028/www.scientific.net/KEM.697.701

8. K. Nakane, S. Matsuoka, S. Gao, S. Yonezawa, J.H. Kim, N. Ogata, Formation of inorganic nanofibers by heat-treatment of poly(vinyl alcohol)-zirconium compound hybrid nanofibers, J. Min. Metall. Sect. B 49 (2013) 77–82.

   https://doi.org/10.2298/JMMB121101027N

9. N. Dharmaraj, C.H. Kim, H.Y. Kim, Synthesis and characterisation of zirconium oxide nanofibers by electrospinning, Synth. React. Inorg. Met.-Org. Nano-Met. Chem. 36 (2006) 29–32. https://doi.org/10.1080/15533170500471391
10. R. Ruiz-Rosas, J. Bedia, J.M. Rosas, M. Lallave, I.G. Loscertales, J. Rodríguez-Mirasol, T. Cordero, Methanol decomposition on electrospun zirconia nanofibers, Catal. Today. 187 (2012) 77–87. https://doi.org/10.1016/j.cattod.2011.10.031
11. Y. Zhao, Y. Tang, Y. Guo, X. Bao, Studies of electrospinning process of zirconia nanofibers, Fibers Polym. 11 (2010) 1119–1122. https://doi.org/10.1007/s12221-010-1119-0
12. C. Shao, H. Guan, Y. Liu, J. Gong, N. Yu, X. Yang, A novel method for making ZrO_2 nanofibres via an electrospinning technique, J. Cryst. Growth. 267 (2004) 380–384. https://doi.org/10.1016/j.jcrysgro.2004.03.065
13. N. Jing, M. Wang, J. Kameoka, Fabrication of ultrathin ZrO_2 nanofibers by electrospinning, J. Photopolym. Sci. Technol. 18 (2005) 503–506. https://doi.org/10.2494/photopolymer.18.503
14. E. Davies, A. Lowe, M. Sterns, K. Fujihara, S. Ramakrishna, Phase morphology in electrospun zirconia microfibers, J. Am. Ceram. Soc. 91 (2008) 1115–1120. https://doi.org/10.1111/j.1551-2916.2008.02264.x
15. S. Singh, V. Singh, M. Vijayakumar, V.V. Bhanu Prasad, Electrospun ZrO_2 fibers obtained from polyvinyl alcohol/zirconium n-propoxide composite fibers processed through halide free sol-gel route using acetic acid as a stabilizer, Mater. Lett. 115 (2014) 64–67.

https://doi.org/10.1016/j.matlet.2013.10.026

16. O. Saligheh, R. Khajavi, M.E. Yazdanshenas, A. Rashidi, Production and characterization of zirconia (ZrO_2) ceramic nanofibers by using electrospun poly(vinyl alcohol)/zirconium acetate nanofibers as a precursor, J. Macromol. Sci. Part B Phys. 55 (2016) 605–616. https://doi.org/10.1080/00222348.2016.1179165
17. L. Li, P. Zhang, J. Liang, S.M. Guo, Phase transformation and morphological evolution of electrospun zirconia nanofibers during thermal annealing, Ceram. Int. 36 (2010) 589–594. https://doi.org/10.1016/j.ceramint.2009.09.030
18. V.V. Rodaev, A.O. Zhigachev, V.V. Korenkov, Y.I. Golovin, The influence of zirconia precursor/binding polymer mass ratio in the intermediate electrospun composite fibers on the phase transformation of final zirconia nanofibers, Phys. Status Sol. A: Appl. Mater. Sci. 213 (2016) 2352–2355. https://doi.org/10.1002/pssa.201600047
19. R.C. Garvie, The occurrence of metastable tetragonal zirconia as a crystallite size effect, J. Phys. Chem. 69 (1965) 1238–1243. http://dx.doi.org/10.1021/j100888a024
20. H. Näfe, D. Gautam, Metastable nanocrystalline zirconia in light of the nucleation theory, J. Phys. Chem. C 120 (2016) 10523–10529. https://doi.org/10.1021/acs.jpcc.6b00512
21. J.R. Kelly, I. Denry, Stabilized zirconia as a structural ceramic: An overview, Dental Mater. 24 (2008) 289–298. https://doi.org/10.1016/j.dental.2007.05.005

22. A.P. Bechepeche, O. Treu Jr., E. Longo, C.O. Paiva-Santos, J.A. Varela, Experimental and theoretical aspects of the stabilization of zirconia, J. Mater. Sci. 34 (1999) 2751–2756. https://doi.org/10.1023/A:1004698026465

23. A.M. Azad, Fabrication of yttria-stabilized zirconia nanofibers by electrospinning, Mater. Lett. 60 (2006) 67–72.

https://doi.org/10.1016/j.matlet.2005.07.085

24. V.V. Rodaev, A.O. Zhigachev, Y.I. Golovin, Microstructure and phase composition of CaO doped zirconia nanofibers, Ceram. Int. 43 (2017) 1200–1204.

https://doi.org/10.1016/j.ceramint.2016.10.063

25. A.B. Suryamas, M.M. Munir, T. Ogi, C.J. Hogan Jr., K. Okuyama, Photoluminescent ZrO_2:Eu^{3+} nanofibers prepared via electrospinning, Jpn. J. Appl. Phys. 49 (2010), art. no. 115003.

https://doi.org/10.1143/JJAP.49.115003

26. G.X. Sun, F.T. Liu, J.Q. Bi, C.A. Wang, Electrospun zirconia nanofibers and corresponding formation mechanism study, J. Alloys Compd. 649 (2015) 788–792.

https://doi.org/10.1016/j.jallcom.2015.03.068

27. K. Castkova, K. Maca, J. Sekaninova, J. Nemcovsky, J. Cihlar, Electrospinning and thermal treatment of yttria doped zirconia fibres, Ceram. Int. 43 (2017) 7581–7587.

https://doi.org/10.1016/j.ceramint.2017.03.050

28. Y. Chen, X. Mao, H. Shan, J. Yang, H. Wang, S. Chen, F. Tian, J. Yu, B. Ding, Free-standing zirconia nanofibrous membranes with robust flexibility for corrosive liquid filtration, RSC Adv. 4 (2014) 2756–2763.

https://doi.org/10.1039/C3RA45043K

29. P. Pokorny, E. Koštáková, F. Sanetmik,P. Mikes, J. Chvojka, T. Kalous, M. Bilek, K. Pejchar, J. Valtera, D. Lukaš, Effective AC needleless and collectorless electrospinning for yarn production, Phys. Chem. Chem. Phys.16 (2014) 26816–26822. https://doi.org/10.1039/c4cp04346d

30. C. Lawson, A. Stanishevsky, M. Sivan, P. Pokorny, D. Lukáš, Rapid fabrication of poly(ε-caprolactone) fibers using needleless alternating current electrospinning, J. Appl. Polym. Sci. 133 (2016) art. no. 43232. https://doi.org/10.1002/app.43232

31. K. Paulett, W.A. Brayer, K. Hatch, T. Kalous, J. Sewell, T. Liavitskaya, S. Vyazovkin, F. Liu, D. Lukáš, A. Stanishevsky, Effect of nanocrystalline cellulose addition on needleless alternating current electrospinning and properties of nanofibrous polyacrylonitrile meshes, J. Appl. Polym. Sci. 135 (2018) art. no. 45772. https://doi.org/10.1002/app.45772

32. A. Stanishevsky, W.A. Brayer, P. Pokorny, T. Kalous, D. Lukáš, Nanofibrous alumina structures fabricated using high-yield alternating current electrospinning, Ceram. Int. 42 (2016) 17154–17161. https://doi.org/10.1016/j.ceramint.2016.08.003

33. R.E. Chinn, Ceramography: Preparation and analysis of ceramic microstructures, ASM International, Materials Park, OH, USA (2002) p.50.

34. K. Nartetamrongsutt, G.G. Chase, The influence of salt and solvent concentrations on electrospun polyvinylpyrrolidone fiber diameters and bead formation, Polymer 54 (2013) art. No. 2166e2173 https://doi.org/10.1016/j.polymer.2013.02.028

35. X.H. Qin, E.L. Yang, N. Li, S.Y. Wang, Effect of different salts on electrospinning of polyacrylonitrile (PAN) Polymer Solution, J. Appl. Polym. Sci. 103 (2007) 3865–3870 https://doi.org/10.1002/app.25498

36. A.M. Drews, L.Cademartiri, G.M. Whitesides, K.J.M. Bishop, Electric winds driven by time oscillating corona discharges, J. Appl. Phys. 114 (2012) 143302. https://doi.org/10.1063/1.4824748

37. J. Scholz, K. Scholz, A.J. McQuillan, In situ infrared spectroscopic analysis of the water modes of $[Zr_4(OH)_8(H_2O)_{16}]_8^+$ during the thermal dehydration of $ZrOCl_2 \cdot 8H_2O$, J. Phys. Chem. A 114 (2010) 7733–7741. https://doi.org/10.1021/jp102589v

38. Y. Zhang, J. Li, Q. Li, L. Zhu, X. Liu, X. Zhong, J. Meng, X. Cao, Preparation of CeO_2–ZrO_2 ceramic fibers by electrospinning, J. Colloid Interface Sci. 307 (2007) 567–571. https://doi.org/10.1016/j.jcis.2006.12.048

39. Z. Qian, J.L. Shi, Characterization of pure and doped zirconia nanoparticles with infrared transmission spectroscopy, Nanostruct. Mater. 10 (1998) 235–244. https://doi.org/10.1016/S0965-9773(98)00062-2

40. H. Zhang, Y. Liu, K. Zhu, G. Siu, Y. Xiong, C. Xiong, Infrared spectra of nanometre granular zirconia, J. Phys.: Condens. Matter. 11 (1999) 2035–2042. https://doi.org/10.1088/0953-8984/11/8/016

41. K.L. Foster, T.E. Caldwell, T. Benter, S. Langer, J.C. Hemminger, and B.J. Finlayson-Pitts, Techniques for quantifying gaseous HOCl using atmospheric pressure ionization mass spectrometry, Phys. Chem. Chem. Phys., 1999, 1, 5615–5621. https://doi.org/10.1039/A907362K

42. L. Li, P. Zhang, J. Liang, S.M. Guo, Phase transformation and morphological evolution of electrospun zirconia nanofibers during thermal annealing, Ceram. Int. 36 (2010) 589–594. https://doi.org/10.1016/j.ceramint.2009.09.030

43. R.C. Garvie, P.S. Nicholson, Phase analysis in zirconia systems, J. Am. Ceram. Soc. 55 (1972) 303–305. https://doi.org/10.1111/j.1151-2916.1972.tb11290.x

44. R. Garvie, M. Goss, Intrinsic size dependence of the phase transformation, temperature in zirconia microcrystals, J. Mater. Sci., 21 (1986) 1253–1257. https://doi.org/10.1007/BF00553259

45. X. Yin, L. Song, X. Xie, Y. Zhou, Y. Guan, J. Xiong, Preparation of the flexible ZrO_2/C composite nanofibrous film via electrospinning, Appl. Phys. A: Mater. Sci. Proc. 122 (2016), art. no. 678. https://doi.org/10.1007/s00339-016-0224-3

46. L.J. Gibson, M.F. Ashby, Cellular solids: structure and properties, 2nd edn. Cambridge, UK: Cambridge University Press (1997).

47. H. Fan, C. Hartshorn, T. Buchheit, D. Tallant, R. Assink, R. Simpson, D.J. Kissel, D.J. Lacks, S. Torquato, C.J. Brinker, Modulus-density scaling behaviour and framework architecture of nanoporous self-assembled silicas. Nature Mater. 6 (2007) 418-423. https://doi.org/10.1038/nmat1913

48. P. Colombo, J.R. Hellmann, D.L. Shelleman, Mechanical properties of silicon oxycarbide ceramic foams, J. Am. Ceram. Soc. 84 (2001) 2245–2251. https://doi.org/10.1111/j.1151-2916.2001.tb00996.x

49. R. G. Munro, Elastic moduli data for polycrystalline ceramics, NISTIR 6853, National Institute of Standards and Technology, Gaithersburg, Maryland 20899 (2002).
50. C.F. Smith, W.B. Crandall, Calculated high-temperature elastic constants for zero porosity monoclinic zirconia, J. Am. Ceram. Soc. 47, (1964) 624–627. https://doi.org/10.1111/j.1151-2916.1964.tb13120.x
51. J. Luo, R. Stevens, Porosity-dependence of elastic moduli and hardness of 3Y-TZP ceramics, Ceram. Int. 25 (1999) 281–286. https://doi.org/10.1016/S0272-8842(98)00037-6
52. W. Pabst, E. Gregorová, G. Tichá, E. Týnová, Effective elastic properties of alumina-zirconia composite ceramics Part 4. Tensile modulus of porous alumina and zirconia, Ceramics − Silikáty 48 (2004) 165–174.
53. C. Bartuli, E. Bemporad, J.M. Tulliani, J. Tirillò, G. Pulci, M. Sebastiani, Mechanical properties of cellular ceramics obtained by gel casting: Characterization and modeling, J. Eur. Ceram. Soc. 29 (2009) 2979–2989. https://doi.org/10.1016/j.jeurceramsoc.2009.04.035
54. A. Kocjan, Z. Shen, Colloidal processing and partial sintering of high-performance porous zirconia nanoceramics with hierarchical heterogeneities, J. Eur. Ceram. Soc. 33 (2013) 3165–3176. https://doi.org/10.1016/j.jeurceramsoc.2013.06.004
55. Z.Y. Deng, J.F. Yang, Y. Beppu, M. Ando, T. Ohji, Effect of agglomeration on mechanical properties of porous zirconia fabricated by partial sintering, J. Am. Ceram. Soc. 85 (2002) 1961–1965. https://doi.org/10.1111/j.1151-2916.2002.tb00388.x

56. A.K. Gain, H.Y. Song, B.T. Lee, Microstructure and mechanical properties of porous yttria stabilized zirconia ceramic using poly methyl methacrylate powder, Scripta Mater. 54 (2006) 2081–2085.

https://doi.org/10.1016/j.scriptamat.2006.03.009

57. Z. Liu, M. G. Scanlon, Scaling Young's modulus of cellular solids, J. Mater. Sci. Lett. 22 (2003) 547– 548.

58. Concise Encyclopedia of the Structure of Materials //Ed. J.W. Martin, Elsevier, Amsterdam (2007) 27–28.

FIGURE CAPTIONS

Figure 1. (a) Electrical conductivity and (b) apparent viscosity of $ZrOCl_2$/PVP precursors with various concentrations of polymer and salt/polymer weight ratios.

Figure 2. (a) Basic schematics of the AFES process; (b–e) Typical appearance of the fibrous flow at different AC rms voltages with a 12.5-mm diameter electrode; (f) As-spun sheet of precursor fibers. Inset: contrast-enhanced photograph of partially aligned strands of fibers in the fibrous sheet. Arrows indicate the direction of collection; (g,h) Nanofibrous ZrO_2 sheet after annealing at 600 ^{o}C.

Figure 3. FTIR spectra of (a) as-spun precursor $ZrOCl_2$/PVP nanofibers with different salt/polymer weight ratios, and (b) ZrO_2 nanofibers after the calcination at 600, 800, and 1000 ^{o}C. Inset: SEM image of 1000 ^{o}C calcined ZrO_2 nanofibrous material with partial alignment of fibers (Arrows indicate the direction of the collector rotation).

Figure 4. DTA/TG/DTG analysis of the decomposition of $ZrOCl_2$/PVP precursor nanofibers with different salt/polymer weight ratios after initial stabilization at 120 ^{o}C. (a) Mass loss curves, (b) DTA/TG/DTG curves for 1.5:1 weight ratio $ZrOCl_2$/PVP precursor fibers.

Figure 5. Average diameter of ZrO_2 nanofibers spun from the 7 wt% solution and calcined at (I) 600 ^{o}C and (II) 1000 ^{o}C, and those spun from the 8 wt% solution and calcined at (III) 600 ^{o}C and

(IV) 1000 ^{o}C. Examples of fiber size distributions for ZrO_2 calcined at 1000 ^{o}C from the $ZrOCl_2$/PVP precursors with 1.5:1 and 2.0:1 weight ratios are shown in inserts.

Figure 6. SEM images of ZrO_2 nanofibers calcined at 600 ^{o}C from the precursor fibers with (a) 1.5:1, (b) 2.0:1 and (c) 2.5:1 salt/polymer weight ratios.

Figure 7. SEM images of nanofibrous ZrO_2 calcined at 1000 ^{o}C from the precursor fibers with (a,d) 1.5:1, (b,e) 2.0:1 and (c,f) 2.5:1 salt/polymer weight ratios. Circles indicate selected fiber segments with the grain size close to fiber diameter.

Figure 8. X-Ray diffraction patterns of ZrO_2 nanofibers prepared from the precursor fibers with different salt/polymer weight ratios by calcination at (a) 600 ^{o}C, (b) 800 ^{o}C, and (c) 1000 ^{o}C.

Figure 9. X-Ray diffraction patterns in 26^{o}–34^{o} 2θ range from nanofibrous ZrO_2 crystallized from $ZrOCl_2$/PVP precursors with 1.5:1 weight ratio: the effect of heating rate and atmosphere.

Figure 10. Examples of strain-stress curves in tensile tests of nanofibrous t-ZrO_2 and m-ZrO_2 meshes with different porosity.

Figure 11. Bending of 0.15 mm-thick nanofibrous ZrO_2 meshes after calcination at (a) 600 ^{o}C and (b) 1000 ^{o}C; (c) A nanofibrous t-ZrO_2 specimen (10-mm gauge length) after the tensile test; (d) Tensile moduli of nanofibrous m-ZrO_2 (*-label) and t-ZrO_2 meshes. Shaded areas indicate the measurement error range. Small red spheres are the flexural moduli data for the same specimens,

and open rhombs are the data from [4,6]. Red dotted curve represents the best fit without the consideration of the change in Young's modulus of nanofibers (C=0.998, C_2=3.6, C_3=1.54, k=1). Purple dash-dot curve is the best fit according to the relationship (6); (e) Young's moduli of various porous zirconia ceramics [47-53] plotted together with different fitting models.

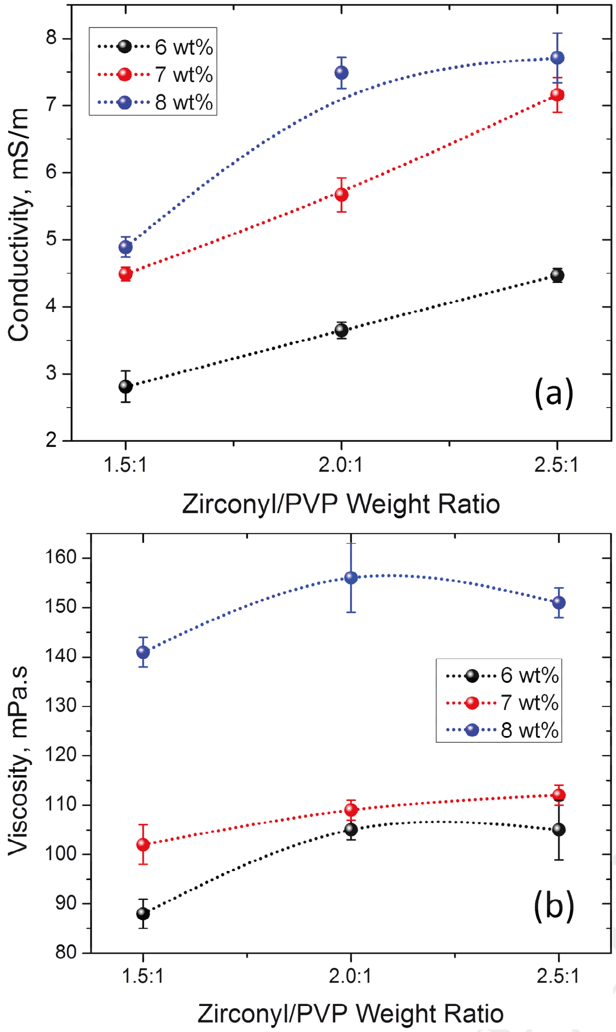
6 wt%
7 wt%
8 wt%
Conductivity, mS/m
2
3
4
5
6
7
8
(a)
1.5:1
2.0:1
2.5:1
Zirconyl/PVP Weight Ratio
Viscosity, mPa.s
80
90
100
110
120
130
140
150
160
(b)
1.5:1
2.0:1
2.5:1
Zirconyl/PVP Weight Ratio

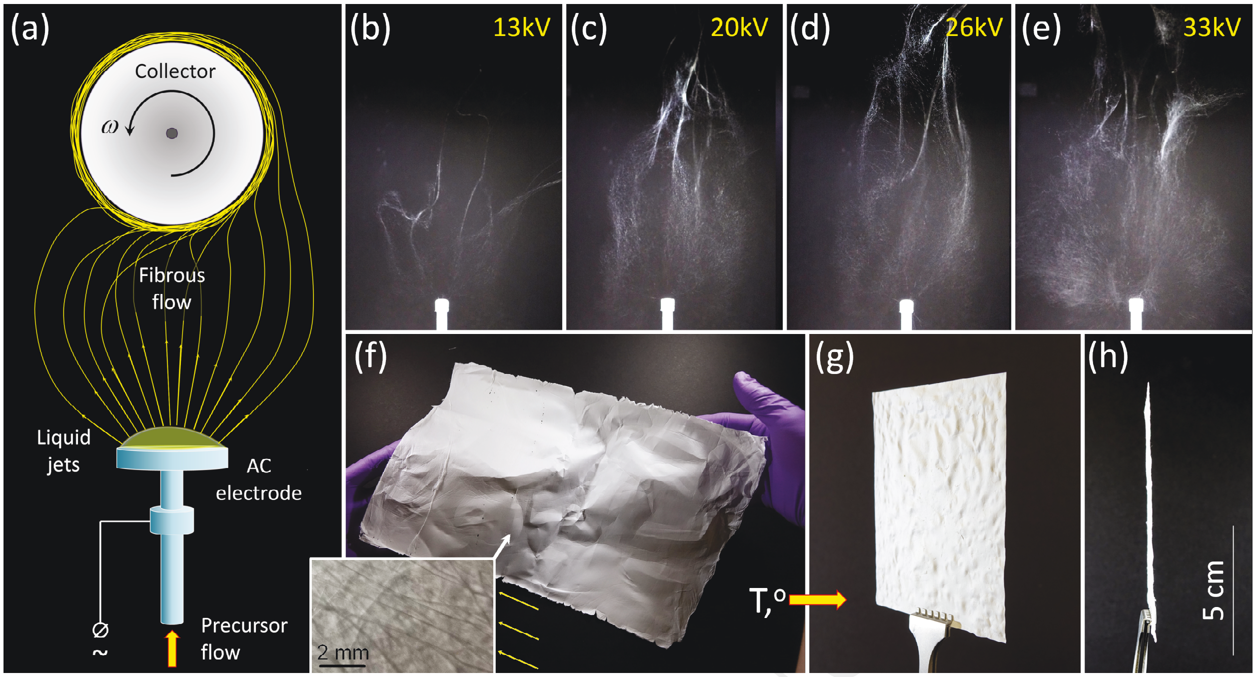
(a)
Collector
ω
Fibrous flow
Liquid jets
AC electrode
Precursor flow
∅
~
(b)
13kV
(c)
20kV
(d)
26kV
(e)
33kV
(f)
2 mm
T,°
(g)
(h)
5 cm

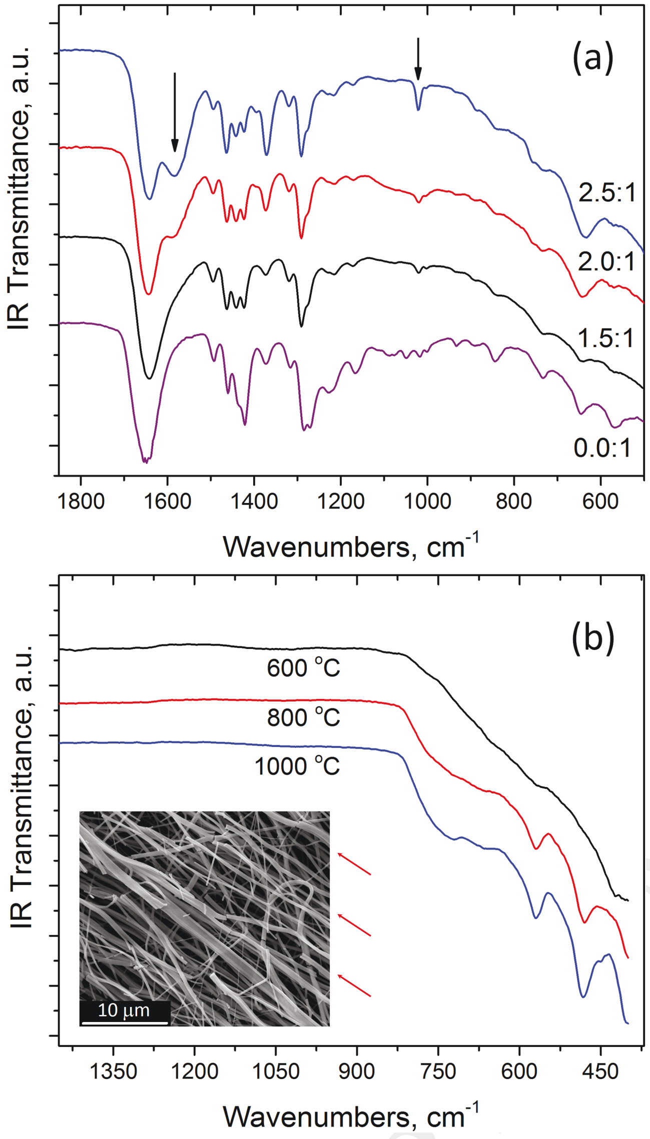
(a)
IR Transmittance, a.u.
2.5:1
2.0:1
1.5:1
0.0:1
1800
1600
1400
1200
1000
800
600
Wavenumbers, cm^{-1}
(b)
IR Transmittance, a.u.
600 °C
800 °C
1000 °C
10 μm
1350
1200
1050
900
750
600
450
Wavenumbers, cm^{-1}

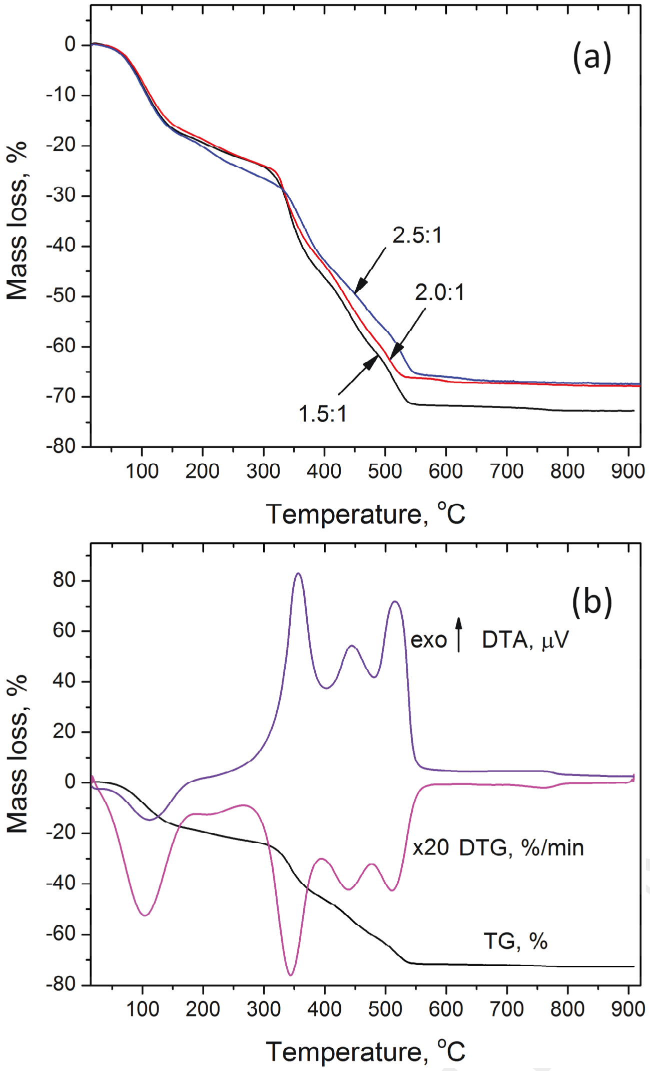
(a)
Mass loss, %
0
-10
-20
-30
-40
-50
-60
-70
-80
2.5:1
2.0:1
1.5:1
100
200
300
400
500
600
700
800
900
Temperature, °C
(b)
Mass loss, %
80
60
40
20
0
-20
-40
-60
-80
exo
DTA, μV
x20 DTG, %/min
TG, %
100
200
300
400
500
600
700
800
900
Temperature, °C

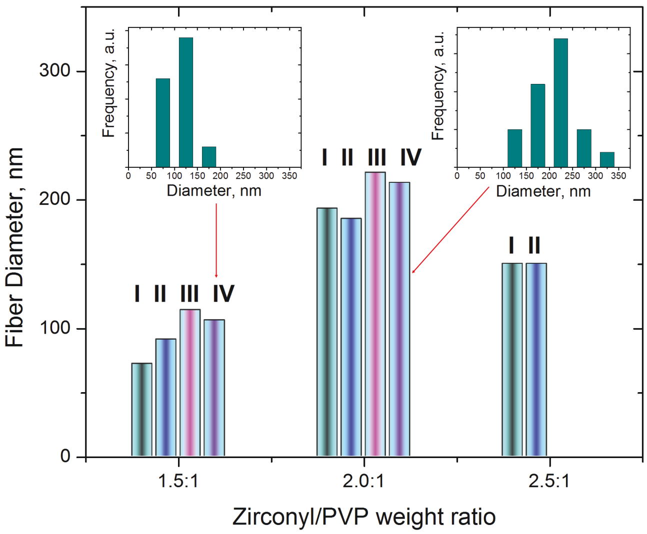
Fiber Diameter, nm
0
100
200
300
1.5:1
2.0:1
2.5:1
Zirconyl/PVP weight ratio
I II III IV
I II III IV
I II
Frequency, a.u.
Diameter, nm
0 50 100 150 200 250 300 350
Frequency, a.u.
Diameter, nm
0 50 100 150 200 250 300 350

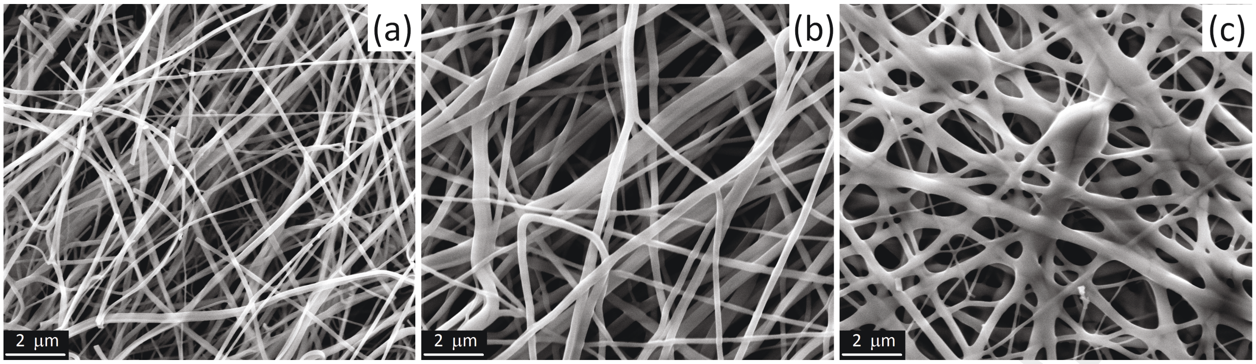
(a)
(b)
(c)
2 µm
2 µm
2 µm

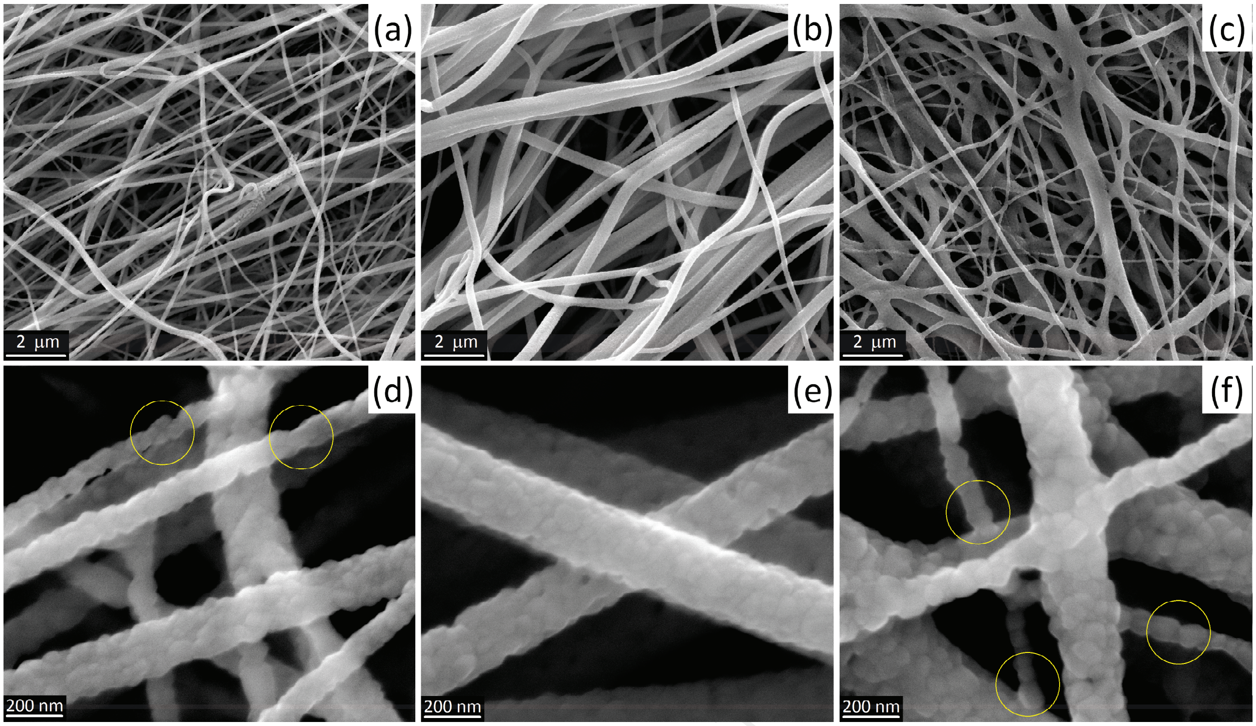
(a)
(b)
(c)
2 μm
2 μm
2 μm
(d)
(e)
(f)
200 nm
200 nm
200 nm

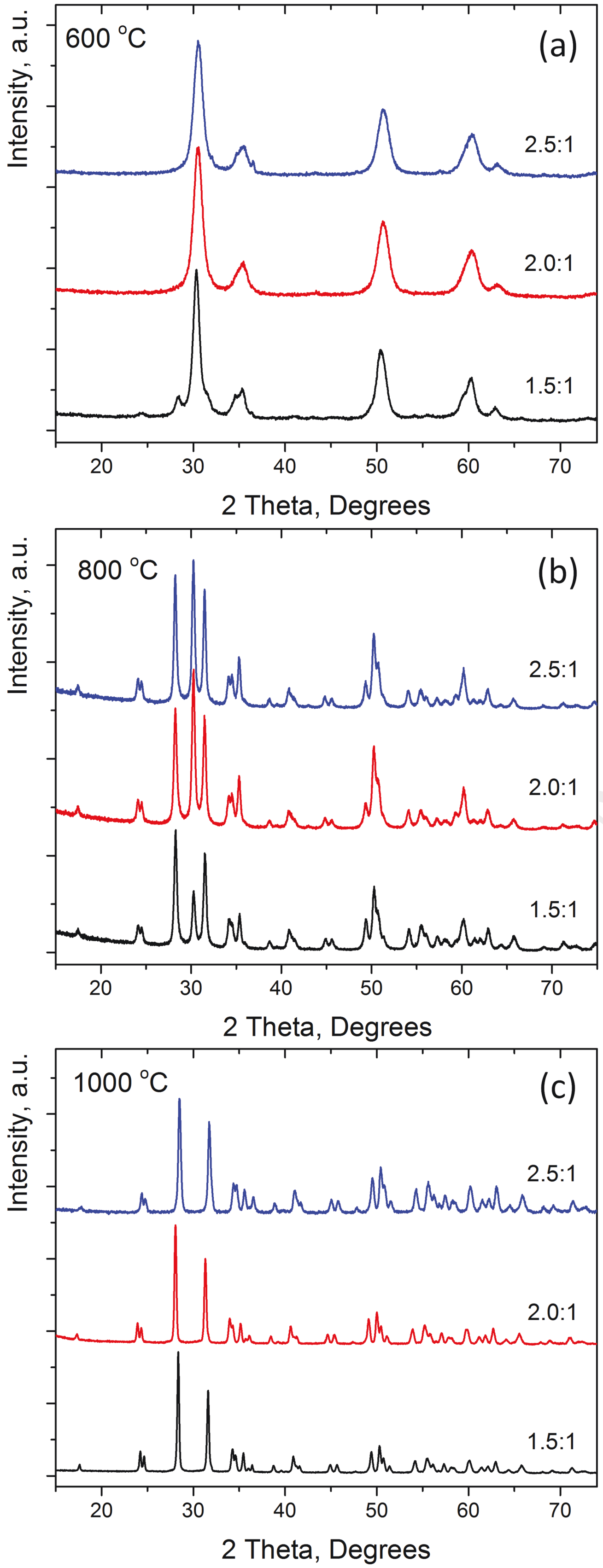
600 °C
(a)
2.5:1
2.0:1
1.5:1
Intensity, a.u.
20
30
40
50
60
70
2 Theta, Degrees
800 °C
(b)
2.5:1
2.0:1
1.5:1
Intensity, a.u.
20
30
40
50
60
70
2 Theta, Degrees
1000 °C
(c)
2.5:1
2.0:1
1.5:1
Intensity, a.u.
20
30
40
50
60
70
2 Theta, Degrees

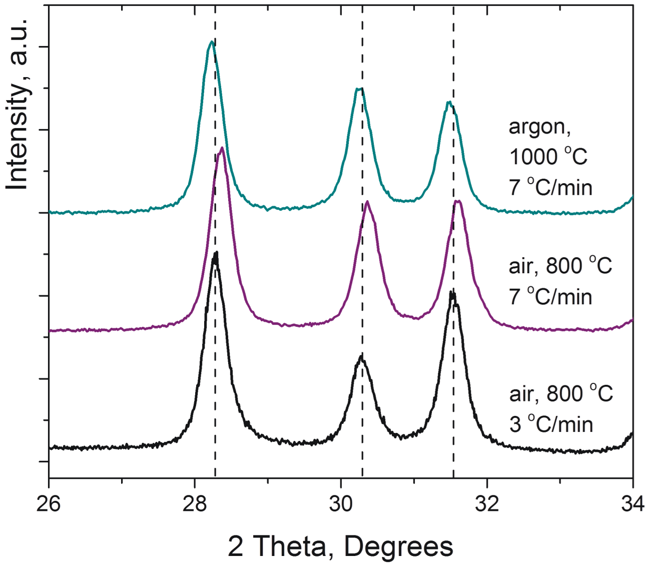
Intensity, a.u.
2 Theta, Degrees
26
28
30
32
34
argon,
1000 °C
7 °C/min
air, 800 °C
7 °C/min
air, 800 °C
3 °C/min

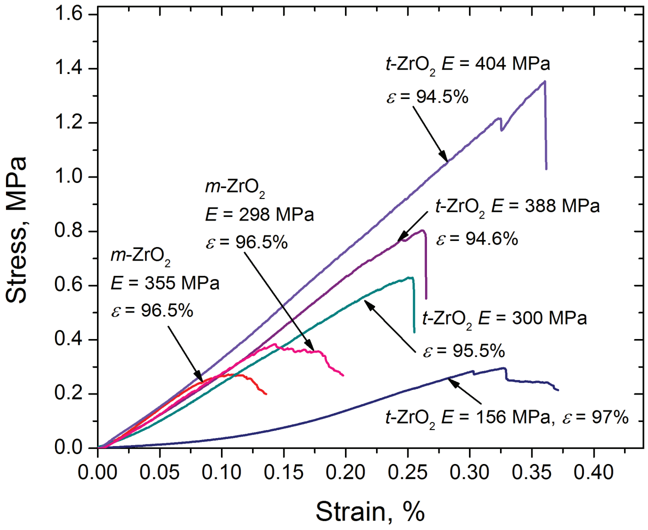
Stress, MPa
Strain, %
1.6
1.4
1.2
1.0
0.8
0.6
0.4
0.2
0.0
0.00
0.05
0.10
0.15
0.20
0.25
0.30
0.35
0.40
t-ZrO$_2$ E = 404 MPa
ε = 94.5%
m-ZrO$_2$
E = 298 MPa
ε = 96.5%
t-ZrO$_2$ E = 388 MPa
ε = 94.6%
m-ZrO$_2$
E = 355 MPa
ε = 96.5%
t-ZrO$_2$ E = 300 MPa
ε = 95.5%
t-ZrO$_2$ E = 156 MPa, ε = 97%

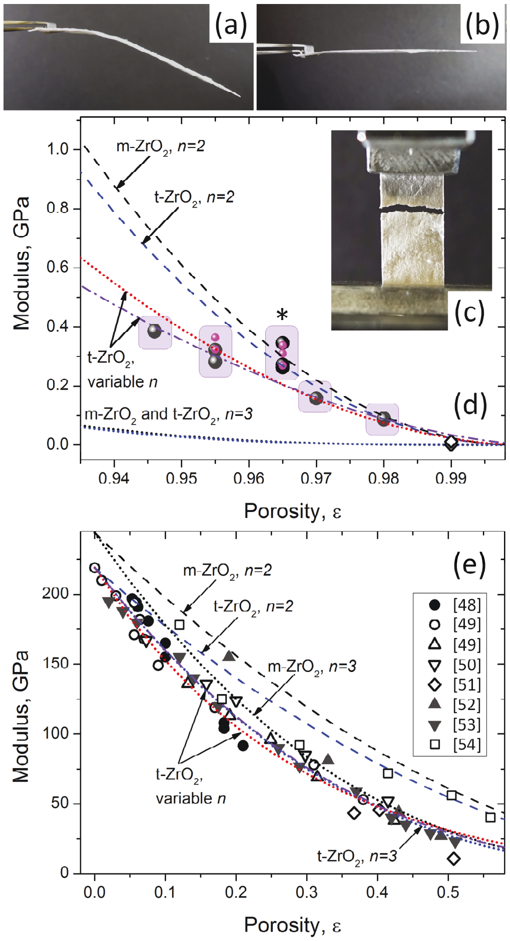
(a)
(b)
(c)
(d)
m-ZrO$_2$, n=2
t-ZrO$_2$, n=2
t-ZrO$_2$, variable n
m-ZrO$_2$ and t-ZrO$_2$, n=3
*
Modulus, GPa
0.0
0.2
0.4
0.6
0.8
1.0
0.94
0.95
0.96
0.97
0.98
0.99
Porosity, ε
(e)
m-ZrO$_2$, n=2
t-ZrO$_2$, n=2
m-ZrO$_2$, n=3
t-ZrO$_2$, variable n
t-ZrO$_2$, n=3
● [48]
○ [49]
△ [49]
▽ [50]
◇ [51]
▲ [52]
▼ [53]
□ [54]
Modulus, GPa
0
50
100
150
200
0.0
0.1
0.2
0.3
0.4
0.5
Porosity, ε